This is the accepted manuscript made available via CHORUS. The article has been published as:

Highly Efficient Broadband Multiplexed Millimeter-Wave Vortices from Metasurface-Enabled Transmit-Arrays of Subwavelength Thickness

Zhi Hao Jiang, Lei Kang, Wei Hong, and Douglas H. Werner

Phys. Rev. Applied **9**, 064009 — Published 8 June 2018

DOI: 10.1103/PhysRevApplied.9.064009

Highly Efficient Broadband Multiplexed Millimeter-wave Vortices from Metasurface-enabled Transmit-arrays of Subwavelength Thickness

Zhi Hao Jiang[1], Lei Kang[2], Wei Hong[1]*, Douglas H. Werner[2#]
[1]*State Key Laboratory of Millimeter Waves, School of Information Science and Engineering, Southeast University,*
Nanjing, 210096, China
[2]*Department of Electrical Engineering, The Pennsylvania State University,*
University Park, PA 16802, USA
*weihong@seu.edu.cn [#]dhw@psu.edu

Structured electromagnetic waves carrying non-vanishing orbital angular momentum (OAM) have recently opened up new frontiers in the field of wave physics, holding great promise for a wide range of potential applications. By leveraging geometric phases originating from spin-to-orbital interaction, spin-dependent wave phenomena can be created, leading to a new realm of dispersionless wave-front manipulation. However, the currently available transmissive vortex beam generators either suffer from a narrow bandwidth, require an optically thick device profile, or are limited by a low efficiency, severely restricting their integration into systems and/or widespread usage for practical applications. Here, we present the design methodology, physical analysis, and complete experimental characterization of a class of millimeter-wave Pancharatnam-Berry transmit-arrays with a thickness of about $\lambda_0/3$, which enables highly-efficient generation and separation of spin-controlled vortex beams over a broad bandwidth, achieving an unprecedented peak efficiency of 88% for a single vortex beam and 71% for dual vortex beams. The proposed transmit-array, which is capable of providing two-dimensional OAM multiplexing and de-multiplexing without normal-mode background interference, overcomes all previous roadblocks and paves the way for high-efficiency electromagnetic vortex beam generation as well as other wave-front shaping devices from microwave frequencies to optical wavelengths.

I. INTRODUCTION

Angular momentum, encompassing spin angular momentum (SAM) and orbital angular momentum (OAM), is one of the most fundamental and important properties of electromagnetic waves, in addition to phase, amplitude, and polarization [1,2]. While SAM is associated with the spin (σ) of a circularly polarized wave, which is intrinsic and directly related to the vectorial nature of light, the OAM is manifested by its annular transverse intensity profile and a corkscrew-shaped phase-front of the beam [3]. Specifically, a structured beam carrying a well-defined OAM, commonly referred to as a “vortex beam”, has a phase dependence of $\exp(-j\ell\varphi)$ in its wave-front, where ℓ represents the topological charge and φ is the polar angle, indicating an OAM of $\ell\hbar$ per photon along the beam axis [4], where $\hbar$ is the reduced Plank constant. Since the initial discovery that beams can carry non-vanishing OAM, there has been a considerable amount of research interest in exploring their intriguing physical properties for potential applications throughout the electromagnetic spectrum [5,6]. This has opened up new frontiers in electrodynamic physics with associated technological advancements in such diverse areas as astrophysical observation [7,8], particle trapping and manipulation [9,10], quantum information processing [11,12], nonlinear optics [13], microcopy [14], microlasers [15], and communications [16-19], to name a few.

The conventional methods for obtaining these OAM beams with exotically structured wave-fronts typically employ transmissive/reflective spiral phase plates [18,20], cylindrical mode converters [21], computer-generated holograms [22], binary gratings [23], gratings based on whispering gallery mode resonators [24], annular arrays of phased antenna elements [25], patch antennas operating at higher order modes [26], and so on. However, all of these techniques either require an optically-large device form factor, necessitate a number of accessory components, or function only within a narrow bandwidth, thus severely restricting their integration into practical systems.

Recently, based on wave-front engineering enabled by quasi-two-dimensional metasurfaces and transmit-/reflect-array concepts, various planar vortex beam generators have been proposed and demonstrated. Rather than relying on optical path difference, the desired aperture field distribution is instead acquired by imposing a spatially-variant abrupt phase change on an incident electromagnetic wave via an array of inhomogeneous subwavelength building blocks [27]. The reflective-mode devices, which have a solid metallic backing layer behind the inhomogeneous metallic or dielectric resonator array with spatially-varying geometries and/or dimensions [28,29], have been reported to provide a single-mode reflected OAM beam from a linearly-polarized incident wave. In contrast, for transmissive-mode vortex generators, a single- and mixed-mode OAM beam was achieved only with a moderate efficiency or a device thickness larger than the wavelength of operation [30-33]. A fundamental limitation of these transmit-/reflect-arrays, which rely on dynamic phase delay, is that the operational bandwidth is very narrow, attributed to the strong dispersion of the employed metallic/dielectric resonators or the Fabry-Pérot resonance associated with thick dielectric gradient index slabs.

In an attempt to address the bandwidth issue, a design concept that exploits the geometric Pancharatnam-Berry (PB) phase was introduced to provide dispersionless phase retardation for circularly-polarized (CP) waves [34,35], which is physically intriguing as it offers a viable path for generating SAM-dependent OAM beams relying on the spin-to-orbital interaction (SOI) [36,37,38]. PB phase metasurfaces have been previously exploited for a number of optical applications including achiral structure enabled optical activity [39,40], integrated spectropolarimeters [41], on chip chiroptical spectroscopy [42], holograms [43], planar lenses [44], and so on. By designing PB devices that operate in the reflective-mode, a high operating efficiency can be achieved, reaching 79% and 63% for single and triple OAM beam generation, respectively [45]. However, for facilitating architectural simplification in the system design and avoiding performance degradation due to blockage, transmissive devices are often preferable. By aligning various types of anisotropic resonators with spatially-varying orientation angles in an array [46-49], subwavelength-thick transmit-arrays have been demonstrated for producing a single-mode CP vortex beam. Multiple OAM beams have also been accomplished by dividing the array into different segments or interleaving the elementary scatters [50,51]. Unfortunately, due to the existence of only the in-plane electric resonance, the total efficiency of these PB transmit-arrays is usually too low for practical applications.

In this work, by cascading together three anisotropic impedance surfaces with custom designed anisotropy and optimizating wave interference in between the layers, we design and realize broadband and high-efficiency functional PB transmit-arrays. Further overlapping the phase masks of a harmonic spatial light modulator and spiral phase plates gives rise to devices enabling multiplexed CP vortex beam generation. Importantly, this allows for independent control of the beam direction, relative intensity, and topological charge for each transmitted vortex beam. Two subwavelength-thick PB transmit-arrays are demonstrated at millimeter-waves, experimentally achieving an efficiency higher than 50% within a broad bandwidth, with a peak efficiency of 88% and 71% for single and dual vortex beam generation, respectively. This disruptive metasurface-enabled technology is expected to pave the way for high-efficiency OAM applications and inspire the emergence of other more complicated wave-front sculpting devices.

FIG. 1. (a) Conceptual configuration of the millimeter-wave PB transmit-array for generating multiple spin-dependent CP vortex beams with independently controllable intensity, direction, and topological charges. Illustrative schematics indicating that the (b) angles (θ_1, θ_2), (c) intensity ratio (I_1/I_2), and (d) topological charges (l_1, l_2) of the outward propagating beams can be controlled independently.

II. RESULTS AND DISCUSSION

A. Multiplexed OAM transmit-array configuration

As shown in Fig. 1(a), the proposed PB transmit-array consists of three metallic layers, each comprised by an array of identical anisotropic resonators with spatially varying orientations, and two thin dielectric spacers. The transmit-array imparts a spatially-dependent abrupt phase change on the transmitted waves but not their amplitudes. When a left-handed circularly-polarized (LCP) wave (*i.e.* $\sigma_{-} = -1$) illuminates the phase-only transmit-array from the **-*z*** direction, a majority of the power will be transmitted with minimal reflection and absorption loss, while transforming it into a right-handed circularly-polarized (RCP) wave (*i.e.* $\sigma_{+} = +1$). The transmitted RCP wave splits into two directive vortex beams pointing in the directions θ_1 and θ_2 off broadside within the *y-z* plane, with topological charges of ℓ_1 and ℓ_2 and peak intensities of I_1 and I_2, respectively. When the polarization of the incident wave is switched from LCP to RCP, the transmitted beams become LCP, with the direction angles mirrored about the *x-z* plane and the sign of the corresponding topological charges flipped. By controlling the orientation of the unit cells, the phase distribution across the aperture of the transmit-array can be tailored, thereby providing a means to independently control the direction and topological charge of each OAM beam, as well as the intensity ratio between the two beams (see Figs. 1(b)-1(d)).

B. Unit cell modeling, design, and analysis

To accomplish such a goal, the unit cells of the transmit-array needs to fullfil simultaneously the handedness conversion and phase delay for CP incident waves. As it is well-known that for an anisotropic medium or structure, the transmitted wave can be expressed using the Jones matrix as $\cos(\psi/2)\,[1, i\sigma_{\pm}] + i\sin(\psi/2)\,[1, i\sigma_{\mp}]e^{i2\sigma_{\pm}\phi_{rot}}$, where ψ is the phase retardation difference between the transmitted waves polarized along the two optical axes. When the optical axis of the anisotropic medium or structure is rotated by an angle ϕ_{rot}, the orthogonally-polarized transmitted CP wave will experience a PB phase change of $\Phi_G = -2\sigma_{\pm}\phi_{rot}$. In particular, when $\psi = \pi$, *i.e.* a half-wave phase retardation, the co-polarized residual component vanishes and the transmitted wave becomes purely orthogonally-polarized, provided that the structural anisotropy is properly controlled [52]. However, an array of resonators with a single metallic layer is not sufficient to achieve such an electromagnetic response since theoretically it only provides a maximal efficiency of 25% [53,54]. Here, inspired by previous arguments on highly-transmissive metallodielectric structures [55-57], the proposed unit cell of the PB transmit-array consists of a three layer structure where each layer contains a single elliptical metallic resonator (see Fig. 2(a)). An I-shaped slot is etched at the center of the elliptical resonators for the purpose of miniaturizing the unit cell size, which is beneficial for improving the resolution of the phase distribution across the transmit-array aperture. The outer, *i.e.* top and bottom, layers have identical patterns, which are different from that of the middle layer.

Due to the fact that each functional layer of the unit cell has different geometries, this triple-layer structure can be understood and designed with the aid of a homogenized model in which each layer was treated as a homogeneous anisotropic impedance surface (AIS) instead of a bulk homogenized effective medium. In our model, the outer and inner AIS layers have surface admittance tensors denoted as $\bar{\bar{\mathbf{Y}}}_{os} = diag[\mathrm{Y}_{osx}, Y_{osy}]$ and $\bar{\bar{\mathbf{Y}}}_{is} = diag[\mathrm{Y}_{isx}, Y_{isy}]$, respectively, with non-vanishing diagonal elements along the optical axis for the resonators [58]. Assuming that the dielectric spacer has a thickness of d_s and a relative permittivity of ε_s, the transmission matrix of the entire triple-layered structure for an ***x***- or ***y***-polarized wave can be expressed as

$$\mathbf{T}_{tot} = \bar{\bar{\mathbf{Y}}}_{so}\begin{bmatrix}\cos(\theta_s) & jZ_s\sin(\theta_s)\\ jY_s\sin(\theta_s) & \cos(\theta_s)\end{bmatrix}\bar{\bar{\mathbf{Y}}}_{si}\begin{bmatrix}\cos(\theta_s) & jZ_s\sin(\theta_s)\\ jY_s\sin(\theta_s) & \cos(\theta_s)\end{bmatrix}\bar{\bar{\mathbf{Y}}}_{so}, \tag{1}$$

where $\bar{\bar{\mathbf{Y}}}_{so(i)} = [1{,}0; \mathrm{Y}_{o(i)sx(y)}, 1]$, $\theta_s = \sqrt{\varepsilon_s}k_0 d_s$, and Z_s (Y_s) is the characteristic impedance (admittance) of the dielectric spacers, respectively. The total transmission matrix $\mathbf{T}_{tot}$ can then be inverted into the scatteirng matrix for the two orthogonal polarizations [59]. In such a way, the transmission amplitude and phase of the structure can be analytically calculated using the model containing three cascaded AISs. Considering a targeted frequency of 30 GHz and a commercially available Taconic TLY-5 laminated substrate material with a thickness of $d_s = 1.52$ mm, the contour plots of the analytically calculated transmission amplitude and phase of the homogenized structure is shown in Figs. 2(b) and 2(c) as a function of $\mathrm{Y}_{osx(y)}/Y_0$ and $\mathrm{Y}_{isx(y)}/Y_0$, where Y_0 is the admittance of free space. A dashed black line was highlighted, tracing out points where the structure provides a near-unity transmission. It can be seen that any pair of two points on this line with a phase difference of 180° can satisfy the desired unit cell response, *i.e.* there is an infinite number of solutions. Taking a closer look at the amplitude and phase distributions allowed us to determine that structures having $Y_{osx(y)}/Y_0$ and $Y_{isx(y)}/Y_0$ closer to 0 have a wider region of high transmission. In this case, no extreme value of $Y_{osx(y)}$ or $Y_{isx(y)}$ is required, which will yield a larger bandwidth when implemented using realistic dispersive structures. Hence, the two red circles were selected, corresponding to $\bar{\bar{Y}}_{os} = \mathrm{diag}[1.05j, -1.15j]Y_0$and $\bar{\bar{Y}}_{is} = \mathrm{diag}[2.15j, -1.70j]Y_0$, which are located at positions almost symmetrical about the center of the high transmission region (*i.e.* the region in yellow color in Fig. 2(b)). Investigations suggested that a thinner or thicker substrate would require a strongly capacitive or inductive surface, respectively, thus limiting the bandwidth (see Supplemental Material, Sec. A [60]). It should also be noted that although substrates with a higher dielectric constant can yield further size and thickness miniaturization, they will significantly introduce more loss at millimeter-waves [61].

FIG. 2. (a) Unit cell geometry of the PB transmit-array composed of three cascaded anisotropic impedance surface layers. The dimensions are: $p_x = p_y = 3.5$, $a_o = 3.15$, $b_o = 2.1$, $r_o = 2.03$, $s_o = 1.09$, $a_m = 2.94$, $b_m = 2.35$, $r_m = 1.56$, and $s_m = 1.17$, all in millimeters. The substrate material is Taconic TLY-5 ($\varepsilon_r = 2.2$, $\delta_{tan} = 0.0009$) with a thickness of $d_s = 1.52$ mm. The bounding layer is Rogers RO4450B ($\varepsilon_r = 3.3$, $\delta_{tan} = 0.004$) with a thickness of $d_b = 0.09$ mm. (b) Analytically calculated transmission amplitude and (c) phase at 30 GHz as a function of both $Y_{isx(y)}/Y_0$ and $Y_{osx(y)}/Y_0$. (d) Retrieved effective surface admittances $Y_{isx(y)}/Y_0$ and $Y_{osx(y)}/Y_0$ for the outer and inner layer metasurfaces. The lumped elements of the equivalanet circuit for the outer and inner (middle) AIS layers along the x- and y-directions are $L_{sox} = 0.55$ nH, $C_{sox} = 11.7$ fF, $L_{pox} = 0.12$ nH, $C_{pox} = 46.3$ fF, $L_{soy} = 0.52$ nH, $C_{soy} = 24$ fF, $L_{poy} = 0.45$ nH, $C_{poy} = 50$ fF, $L_{smx} = 0.3$ nH, $C_{smx} = 21.1$ fF, $L_{pmx} = 0.1$ nH, $C_{pmx} = 52.3$ fF, $L_{smy} = 0.48$ nH, $C_{smy} = 28.5$ fF, $L_{pmy} = 0.6$ nH, $C_{pmy} = 43.4$ fF. (e) Simulated/theoretical transmittance and transmission phase of the unit cell as a function of rotation angle (ϕ_{rot}) at 29.3, 30, and 32.1 GHz. Linear polarization transmission amplitudes and phases for the (f) outer and (g) inner layer of metasurfaces.

In order to achieve the required surface admittance tensor for each layer, which has complementary responses, *i.e.* one capacitive ($\mathrm{Im}\{Y_{o(i)s}\} > 0$) and the other inductive ($\mathrm{Im}\{Y_{o(i)s}\} < 0$), along the two orthogonal optical axes, the aspect ratio of the slot loaded resonators were optimized for controlling the degree of anisotropy. In addition, since the response of an AIS is inherently dispersive, a geometry-induced circuit model, which consists of a parallel LC connected in series with a series LC (see the inset of Fig. 2(d)), was used to model the frequency-dependent $Y_{o(i)sx(y)}$ of the outer and inner AIS layers. Basically, for each layer, the gap in between adjacent unit cells provides a capacitance C_s, while the metallic portions of the elliptical patch can be represented by an inductance L_s. The I-shaped slot at the center of the patch can be represented as a parallel LC resonator with L_p and C_p. By optimizing the geometrical dimensions of the resonators via parametric studies, which tailors the dispersion of the effective surface admittance, a wide operational bandwidth can be achieved. The normalized effective surface admittance tensor elements for the outer and inner layers, retrieved from scattering parameters at normal incidence [62,63], are displayed in Fig. 2(d), along with the values of the lumped elements of the circuit model for the outer and inner AIS layers (see caption). It can be seen that at the targeted frequency, the effective surface admittances of the discrete AIS meet the requirement dictated by the theoretical model with negligible real parts, indicating an extremely low loss. Moreover, in the frequency range from 29 to 32 GHz, the values of the effective surface admittances are slowly varying, especially the components along the x-direction, *i.e.* $Y_{o(i)sx}$, implying that as frequency deviates from the targeted 30 GHz, the response of the structure will still be well-maintained.

As shown in Fig. 2(b), the T_{LR} and T_{RR} curves of the realistic structure, obtained from a full-wave high frequency structure simulator (HFSS) solver, are plotted as a function of rotation angle. For the orthogonally-polarized CP transmitted wave, the phase delay has a dispersionless linear dependence on ϕ_{rot}, indicating that a stable phase distribution can be formed over a wide bandwidth. This physically originates from the geometrical nature of the Berry phase difference, which is equal to half of the area enclosed by the two geodesic lines when a RCP incident wave (*i.e.* the north pole of the Poincare sphere) is transformed into a LCP wave (*i.e.* the south pole of the Poincare sphere) by passing through structures with a rotation angle difference of ϕ_{rot}. Regarding the transmittance, T_{LR} is more than 80% over a wide frequency range from 29.3 to 32.1 GHz with a peak value of 94% at 30 GHz, while T_{RR} is less than 10%, meaning that a majority of the incident RCP wave is transformed into a LCP wave and vice versa due to reciprocity. It should be noted that T_{LR} remains higher than 50% over a broad bandwidth of nearly 19% (see Supplemental Material, Sec. A [60]). A design with the same geometry but operating at the mid-infrared regime was also considered, which achieves a peak T_{LR} of about 63% at 4 μm and a T_{LR} > 50% bandwidth of 10%, showing its promise for various transmissive optical applications (see Supplemental Material, Sec. B [60]).

The CP transmittance and phase curves calculated analytically using the retrieve dispersive effective surface admittance tensors and coordinate rotation transformation matrix are also shown in Fig. 2(e). The strong agreement between the full-wave and analytical results validates the multilayer AIS homogenization model. It reveals the fact that the interaction between layers are primarily wave interference instead of strong evanescent coupling manifested by a magnetic resonance [61]. A detailed examination of the transmission amplitude and phase for $\boldsymbol{x}$- and $\boldsymbol{y}$-polarized waves of the individual outer and inner layers also confirms the physical mechanism of the tri-layer transmit-array. As revealed by Fig. 2(f) and 2(g), all three AIS layers have a transmission ($|t_{xx(yy)}| > 0.8$) due to their small reactance, *i.e.* $|Y_{o(i)sx(y)}| \leq 2.5$, in a wide frequency range such that the behavior of the AIS is not close to a "short circuit". For each AIS, the capacitive response along the x-direction ($\text{Im}\{Y_{o(i)sx}\} > 0$) causes a phase lag while the inductive response along the y-direction ($\text{Im}\{Y_{o(i)sy}\} < 0$) leads to a phase advance. The transmission phase along the y-direction is ahead of that along the x-direction by about $\Delta\varphi_o \approx 60°$ and $\Delta\varphi_i \approx 80°$ for the outer and inner layers, respectively. Summing up the phase differences for all three layers results in $\Delta\varphi = 2\Delta\varphi_o + \Delta\varphi_i \approx 200°$, which is close to a half-wave phase difference. Since each layer does not have perfect transmission, *i.e.* they are partially reflective, the interference between them was exploited during the design to achieve a good impedance match as well as a transmission phase difference modification such that $\Delta\varphi \approx 180°$ in the band of interest.

C. Design, fabrication, and characterization of spin-dependent single vortex-beam transmit-array

With the designed unit cell, optically-thin planar devices for highly-efficient and wideband wave-front control can be created by imparting a spatially-varying phase gradient for transmitted CP waves, which bends the wave towards the direction of a particular diffraction mode with a high purity (see Supplemental Material, Sec. C [60]). In order to verify such capability, first, a single-beam transmit-array for simultaneous spin-dependent vortex-beam generation and separation was designed and fabricated (see Fig. 3(a)) with a distribution of $\phi_{rot}(x, y)$ expressed as

$$\phi_{rot}(x,y) = -[(\pi/n_{sc}p)y - \ell\varphi/2], \tag{2}$$

where $n_{sc} = 10$ and $\ell = 1$ such that the beam direction is pointing at $k_x = 0$, $k_y/k_0 = -\sigma_{i\pm}\lambda_0/10p$ with $\sigma_{i\pm}$ denoting the spin of the incident wave.

The fabricated sample was characterized using a near-field measurement system in an anechoic chamber. In the measurement setup, RCP and LCP horn antennas operating in the frequency range of interest were used as the source for emitting RCP and LCP waves that illuminate the transmit-array sample (see Supplemental Material, Sec. D [60]). A linearly-polarized Ka-band open rectangular waveguide was used as the near-field probe for recording the complex transmitted field in a plane at a distance of 3 cm away from the output interface of the sample. The linearly-polarized probe was employed to record both x- and y-polarized complex field quantities by rotating it 90° about its center. The measured vectorial near-field results were then utilized to deduce the far-field intensity and phase patterns based on the free-space dyadic Green's function [59].

FIG. 3. (a) Photograph of the fabricated single vortex beam PB transmit-array. (b) Simulated and measured efficiency of the transmit-array as a function of frequency when illuminated by a LCP and a RCP wave. Normalized measured LCP and RCP components of the near-field (c) intensities and (d) phases at a plane 3 cm away from the output interface of the PB transmit-array at 29.4 GHz. Normalized measured LCP and RCP components of the far-field (e) intensities and (f) phases of the transmitted wave of rotation angle (ϕ_{rot}) at 29.3, 30, and 32.1 GHz. Linear polarization transmission amplitudes and phases for the (f) outer and (g) inner layer of metasurfaces.

The intensity and phase distributions of the RCP and LCP components of the normalized measured near-field of the PB transmit-array, are displayed in Figs. 3(c) and 3(d), for both RCP and LCP incident waves at 29.4 GHz. It can be observed that the results agree strongly with simulated results (see Supplemental Material, Sec. E and Sec. F [60]). The orthogonally-polarized components of the transmitted fields exhibit a circular periphery outlining the shape of the aperture with a null at the center, which clearly indicates the existence of an optical singularity even in the near-field region very close to the aperture. The phase distributions of the orthogonally-polarized components of the transmitted fields possess fork-like patterns, with the bifurcation located at a position coinciding with the intensity null. The normalized measured far-field patterns for both the LCP and RCP components (see Figs. 3(e) and 3(f)) indicate that the orthogonally-polarized OAM beams are well separated with a negligible co-polarized residual beam pointing at broadside, indicating simultaneous achievement of both optical singularity and spin-Hall effect with a high efficiency [64]. Importantly, the transmit-array protytype accomplished a high efficiency of more than 50% within a broad bandwidth of 17% with a peak value of 88% (92% in simulation) (see Fig. 3(b)), far superior to the current state-of-the-art microwave and optical OAM beam generators [28-33,45-51]. The efficiency was defined by the ratio of the sum of the power associated with all the desired OAM beams to that of the resulting beam when the transmit-array is absent, *i.e.* the plane wave passing through the empty aperture, which can be calculated using either the simulated or measured far-field quantities. Comparing to previous experimental demonstrations of OAM generators at low frequencies, which only reported a partial characterization by recording a certain field component within a small region in the near-field [20,21,33,61] or the intensity in the far-field [25], the measurement performed here allowed us a full characterization of the entire OAM generator.

D. Demonstration of spin-dependent dual vortex-beam transmit-arrays with independent controllability

Multiple controllable vortex beam generation with a single transmissive device is of great importance in a wide variety of applications including high speed communication systems based on OAM, simultaneous tracking of multiple particles, and so on. By incorporating spiral phase profiles into a harmonic-response spatial light modulator with tailored intensity [65], a spin-dependent dual OAM beam generator corresponding to that displayed in Fig. 1 was designed. The distribution in the rotation angle $\phi_{rot}(x,y)$ corresponding to the tiling of unit cells across the quasi-circular aperture is represented by

$$\phi_{rot}(x,y) = -arg\left(\sum_{m=1}^{2} a_m e^{jp_m} e^{-j\left[\left(\frac{\pi}{n_{scm}p}\right)y+\ell_m\varphi/2\right]}\right), \tag{3}$$

where a_m and p_m represent the amplitude and phase of each desired diffraction order (see Fig. 4(a)). Such a duplicator provides a diffraction efficiency reaching 81%. For the two transmitted OAM beams, which are confined within the y-z plane, the pointing directions correspond to $k_x = 0$, $k_{y1}/k_0 = -\sigma_{i\pm}\lambda_0/n_{sc1}p$ and $k_{y2}/k_0 = -\sigma_{i\pm}\lambda_0/n_{sc2}p$ with topological charges of ℓ_1 and ℓ_2, respectively, where $\sigma_{i\pm}$ denotes the spin of the incident wave. Since a beam with a higher order OAM naturally has a lower peak intensity, such a method can serve to precisely control the field strength for particle manipulation and to balance the signal-to-noise ratio for multiple receivers among the generated vortex beams with different topological charges. The parameter p_m can be optimized to maximize the efficiency of the finite-sized transmit-array and to a certain extent improve the overall beam quality. As a proof-of-concept example, the design parameters were properly chosen such that the resulting PB transmit-array can generate two CP vortex beams pointing at $\theta_{t1} = \sigma_{i\pm} \sin^{-1}[-\lambda_0/8p]$ and $\theta_{t2} = \sigma_{i\pm} \sin^{-1}[\lambda_0/23p]$, while possessing the same peak intensity and topological charges of $\ell_1 = 2\sigma_{i\pm}$ and $\ell_2 = -\sigma_{i\pm}$, respectively. It should be noted that multiple OAM beams can also be realized by dividing the transmit-array into different segments or interleaving several groups of unit cells each producing a single beam [50,51]; however, these methods suffer from a significantly reduced overall efficiency as compared to a harmonic-response PB transmit-array.

FIG. 4. (a) Distribution of the rotation angle (ϕ_{rot}) of the unit cells for generating spin-dependent dual-mode CP OAM beams with high efficiency. (b) Photograph of the fabricated PB transmit-array sample. Normalized measured LCP and RCP components of the near-field (c) intensities and (d) phases at a plane 3 cm away from the output interface of the PB transmit-array at 29.4 GHz. Normalized simulated LCP and RCP components of the near-field (e) intensities and (f) phases at a plane 3 cm away from the output interface of the PB transmit-array at 30 GHz.

Figure 4(b) shows the fabricated PB transmit-array for dual OAM beam generation. The normalized measured near-field intensity and phase distributions of the RCP and LCP components at 29.4 GHz are displayed in Figs. 4(c) and 4(d), for both RCP and LCP incident waves. The co-polarized components have a near-zero intensity and a flat distribution, meaning that the spin is almost entirely flipped as the CP incident wave passes through the transmit-array and the unit cells with different rotation angles have no effect on the phase of the co-polarized waves. Interference intensity and phase patterns can be observed within a circular area, exhibiting a complicated quad-furcating pattern at the central region. From the normalized measured far-field intensity and phase patterns of the LCP and RCP components (see Figs. 5(a) and 5(b)), two well-separated RCP OAM-carrying beams with donut-shaped intensity profiles and helical phase-fronts can be observed for a LCP incident wave, possessing topological charges of ℓ = -2 and ℓ = +1 and pointing at $k_{y1}/k_0 = 0.361$ and $k_{y2}/k_0 = -0.127$, respectively. The measured radius ratio between the two modes is about 0.72, which agrees well with the theoretical value of $1/\sqrt{2}$ [1]. For a RCP incident wave, the sign of the topological charges as well as the directions of the two beams are flipped, due to the inherent spin-dependent property of the geometric phase. Importantly, the intensities of the two OAM beams, although corresponding to different modes, are about the same (see Fig. 5(e)). Deep nulls can be identified at the center of the two vortex beams, which indicates the formation of high-quality optical singularities in both beams. The dual OAM beam transmit-array achieves a measured peak efficiency of 71% (see Fig. 5(f)), with an efficiency > 50% bandwidth of about 13%, which is a consequence of the wideband high transmittance of the cross-polarized wave and the dispersionless phase retardation of the employed Berry phase. In particular, even at non-optimal frequencies within this band, the normal co-polarized mode will be radiated in the broadside direction, which will not interfere with the vortex beams, thus ensuring a higher mode purity as compared to vortex beams produced at the normal angle [20,31,33,47,60]. Hence, this work represents a major step forward in the state-of-the-art of multiplexed spin-dependent OAM beam generation with a sub-wavelength thick transmissive device.

FIG. 5. Normalized measured LCP and RCP components of the far-field (a) intensities and (b) phases of the transmitted beam. Normalized simulated LCP and RCP components of the far-field (c) intensities and (d) phases of the transmitted beam. (e) Simulated and measured normalized far-field intensities of transmitted RCP and LCP waves as a function of k_y/k_0 in the *y-z* plane, *i.e.* $k_x = 0$. (f) Simulated and measured efficiency of the transmit-array as a function of frequency when illuminated by a LCP and a RCP wave.

Simulations were conducted to confirm the wave-front shaping phenomena observed in experiments. Both the normalized simulated near-field (see Figs. 4(e) and 4(f)) and far-field (see Figs. 5(c) and 5(d)) intensity and phase patterns agree strongly with their respective measured counterparts. The simulated efficiency profile as a function of frequency, which exhibits a peak efficiency of 76% at 30 GHz, indicates a slight frequency shift of about 2% as compared to the measured result due to fabrication inaccuracies (see Fig. 5(f)). It should be noted that, by modifying the design parameters associated with each beam, the beam direction and topological charge of each vortex beam can be independently controlled, as shown in Figs. 6(a)-(d) (see Supplemental Material, Sec. G [60]). In addition, as shown in Fig. 6(e), the intensity ratio between the two beams can also be changed to almost any desired value (see Supplemental Material, Sec. G [60]).

FIG. 6. (a) The direction of the first beam with a topological charge of ℓ = -2 (or +2) is independently changed to k_y/k_0 = +0.57 (or -0.57). (b) The direction of the second beam with a topological charge of ℓ = +1 (or -1) is independently changed to k_y/k_0 = -0.48 (or +0.48). (c) The topological charge of the first beam is independently changed to have ℓ = -3 (or +3). (d) The topological charge of the second beam is independently changed to have ℓ = +2 (or -2). (e) The intensity ratio of the two beams is changed to be 4:1.

E. Two-dimensional multi-stream vortex beam multiplexing and de-multiplexing

The subwavelength-thick PB transmit-array demonstrated above, which generates two independently controllable OAM beams within the *y-z* plane, can be further extended to achieve two-dimensional (2D) massive vortex beam multiplexing and de-multiplexing. This represents a critical step towards the successful implementation of future OAM-based millimeter-wave communication and sensing/detecting systems [66]. In this case, the PB transmit-array possesses a distribution of unit cells with the rotation angle $\phi_{rot}(x,y)$ across the quasi-circular aperture represented by

$$\phi_{rot}(x,y) = -arg\left(\sum_{m=1}^{4} a_m e^{jp_m} e^{-j\left[\left(\frac{\pi}{n_{scxm}p}\right)x+\left(\frac{\pi}{n_{scym}p}\right)y+\ell_m\varphi/2\right]}\right), \tag{4}$$

where n_{scxm} and n_{scym} control the angular relation between the incident and transmitted beams, while ℓ_m determines the topological charge of each transmitted beam. When an incident RCP/LCP beam, denoted as $Sm_{iR(L)}$, illuminates the transmit-array at an angle $\sigma_{i\pm}\, k_{xm}/k_0 = \sigma_{i\pm}\, \lambda_0/n_{scxm}p$, $\sigma_{i\pm}\, k_{ym}/k_0 = \sigma_{i\pm}\, \lambda_0/n_{scym}p$, where $\sigma_{i\pm}$ represents the spin of the incident wave and $m = 1, \dots, 4$, four vortex beams will be generated each pointing in a distinct direction. By controlling the added transverse momentum imposed on the incident wave, a LCP/RCP vortex beam with the desired topological charge of $\sigma_{i\pm}\ell_m$ can be steered at a direction normal to the output interface of the transmit-array (see Fig. 7(a)). The other resulting OAM beams will emanate in directions far-away from the normal angle and even fall entirely outside the visible region of the *k* space. In such a way, multiple uncorrelated signal beams, each carrying a data stream, can be combined into a single beam with mixed but separable OAM modes, thereby achieving a highly desirable 2D multiplexing functionality.

For the same transmit-array, when imposing a certain OAM on the incident wave such that the device is illuminated by a normally incident LCP/RCP OAM beam carrying a topological charge of $-\sigma_{i\pm}\ell_m$, the topological charge of the multiple transmitted wave will change accordingly. In such a circumstance, only the one pointing at the outcoming angle of $(-\sigma_{i\pm}\, k_{xm}/k_0,\, -\sigma_{i\pm}\, k_{ym}/k_0)$ is a plane-wave-like beam with a vanishing topological charge. All the other outcoming beams will have higher order OAM modes, thus possessing a much weaker peak intensity (see Fig. 7(c)). This indicates that an incident beam with mixed OAMs can be separated by such a PB transmit-array into directive plane-wave-like beams pointing in angularly resolvable directions, thus providing a de-multiplexing functionality. It should be noted that these two functionalities, *i.e.* multiplexing and de-multiplexing, are equivalent to the generation of multiple OAM beams from a single normally incident plane wave as we have previously demonstrated. This equivalence is due to the principle of transverse and angular momentum exchange between the transmit-array and propagating electromagnetic waves. Importantly, the residual beams, *i.e.* the transmitted beams with the same spin as that of the incident wave, are pointing in directions well-separated from the desired beams. Hence, by virtue of the spin-determined properties enabled by controlling the geometric phase, simultaneous OAM and polarization multiplexing/de-multiplexing can be achieved using a single PB transmit-array. This provides a compact and low-cost solution as compared to previously employed approaches that either adopt a distinct pair of OAM beam converters for each signal beam or utilize bulky all-dielectric mode converters [18,19].

As an example, by employing the proposed unit cell design, a PB transmit-array allowing for octa-beam multiplexing/de-multiplexing was designed and numerically validated, which utilizes the two orthogonal circular polarizations and four OAM modes. The parameters n_{scxm} and n_{scym} were selected such that the beams $S1_{i(o)L(R)}$ and $S2_{i(o)L(R)}$ are confined within the *x*-*z* plane, while the beams $S3_{i(o)L(R)}$ and $S4_{i(o)L(R)}$ are bounded within the *y*-*z* plane, with $k_{x1}/k_0 = k_{y3}/k_0 = 0.71$, $k_{x2}/k_0 = k_{y4}/k_0 = -0.52$, and $k_{y1} = k_{y2} = k_{x3} = k_{x4} = 0$ at 30 GHz. The topological charge parameters were selected to be $-\ell_1 = \ell_3 = 2$ and $\ell_2 = -\ell_4 = 4$. Hence, this design is basically a 2D extension of the dual OAM beam generator. As can be seen from the normalized simulated far-field intensity and phase patterns displayed in Fig. 7(b), the RCP/LCP incident beams, confined within the *x*-*z* plane and designated as $S1_{iR(L)}$ and $S2_{iR(L)}$, produce LCP/RCP OAM beams with topological charges of $-2\sigma_{i\pm}$ and $4\sigma_{i\pm}$, respectively. Conversely, the incident beams $S3_{iR(L)}$ and $S4_{iR(L)}$ within the *y*-*z* plane produce LCP/RCP OAM beams with topological charges $2\sigma_{i\pm}$ and $-4\sigma_{i\pm}$, respectively. In fact, for each incident beam, four output beams will be generated. By enforcing a large angular separation between them, the three remaining undesired beams can be positioned in directions far from broadside that are outside the angular region of interest, thereby ensuring a clean diffraction pattern. Consequently, the output beam has a far-field pattern featuring a well-defined single OAM mode at the center of the momentum space. Only a minor spurious OAM beam can be observed near the edge of the visible region due to the smaller angular separation between the output OAM beams with topological charges of $\pm 4\sigma_{i\pm}$.

FIG. 7. (a) Conceptual configuration of the PB transmit-array for encoding 8 CP incident beams into a multiplexing mixed-mode vortex beam. (b) Normalized simulated orthogonally-polarized component of the far-field intensities and phases of the transmitted beam at 30 GHz due to incident beams Sm_{iR} and Sm_{iL}, where $m = 1, \dots, 4$, respectively. (c) Conceptual configuration of the PB transmit-array for de-multiplexing a beam with mixed OAM modes into 8 CP transmitted beams. (d) Normalized simulated orthogonally-polarized component of the far-field intensities and phases of the transmitted beams Sm_{oR} and Sm_{oL} at 30 GHz, where $m = 1, \dots, 4$, respectively, due to an incident OAM beam with a topological charge and polarization corresponding to that shown in (b).

As the normalized simulated far-field intensity and phase patterns reported in Fig. 7(d) show, when a LCP/RCP OAM beam illuminates the transmit-array at normal incidence, the desired transmitted beam, with a vanishing OAM, is refracted into different angles depending on the topological charge and spin of the incident wave. In addition to this plane-wave-like beam, there are three other higher order OAMs beams with a much weaker intensity and a null at the beam center, which will not affect the signal-to-noise ratio when the desired plane-wave-like beam is being detected. Specifically, for LCP/RCP incident OAM beams with topological charges $2\sigma_{i\pm}$ and $-2\sigma_{i\pm}$, the resulting RCP/LCP transmitted beams, which are confined within the principle planes and denoted as $S1_{oR(L)}$ and $S3_{oR(L)}$, respectively, are pointing in directions that are $0.71k_0$ away from the center of the momentum space. The three residual OAM beams have topological charges with absolute values of 2, 4, and 6, respectively, as demonstrated by the phase distributions shown in Fig. 7(d). As a comparison, for LCP/RCP incident OAM beams with smaller topological charges $4\sigma_{i\pm}$ and $-4\sigma_{i\pm}$, the resulting transmitted beams are directed at angles that are $0.52k_0$ away from the center of the momentum space. The three residual OAM beams in this case have topological charges with absolute values of 2, 6, and 8, respectively. This confirms that the proposed ultrathin millimeter-wave PB transmit-array has the capability of processing multiple signals by multiplexing them into a mixed-mode vortex beam as well as de-multiplexing a beam with mixed OAM indices to recover the original signal beams and to separate them in the momentum space. It should be noted that for both the multiplexing and de-multiplexing case, the reflection loss is less than 5% and the power that couples into the desired mode is about 19%, which is still higher than many of the reported transmissive single-mode OAM beam generators.

III. CONCLUSION

In conclusion, we have presented a metasurface-based approach for designing high-efficiency and broadband PB transmit-arrays operating in the millimeter-wave band that are capable of producing a single or multiple spin-dependent OAM-carrying beams. This was achieved by incorporating three cascaded layers of anisotropic impedance surfaces composed of an array of resonators with tailored wave interference in between the layers and utilizing the geometric phase via variable rotation of the unit cells. Two subwavelength-thick PB transmit-arrays for highly-efficient spin-dependent multiplexed OAM beam generation and separation free from normal-mode background interference were demonstrated, along with independently controllable direction, topological charge, and intensity ratio for each beam. The phase-only OAM multi-beam transmit-array, which is capable of fulfilling 2D simultaneous polarization and OAM multiplexing and de-multiplexing, will have a profound impact on future OAM-based systems and is expected to inspire the creation of other advanced metasurface-enabled electromagnetic structures with unconventional wave-fronts.

ACKNOWLEDGMENTS

This work was funded by the Natural Science Foundation of Jiangsu Province under Grant BK20170687, the Natural Science Foundation of China (NSFC) under Grant 61627801, the Fundamental Research Funds for Central Universities of China under Grant 3204007201, and the Penn State MRSEC, Center for Nanoscale Science, under the award NSF DMR-1420620. Partial support from the Penn State University John L. and Genevieve H. McCain endowed chair professorship is also gratefully acknowledged.

---

[1] L. Allen, S. M. Barnett, and M. J. Padgett, *Optical Angular Momentum*, (Taylor and Francis Group, Abingdon, UK, 2003).

[2] J. P. Torres and L. Torner, *Twisted Photons: Applications of Light with Orbital Angular Momentum*, (Wiley, Hoboken, NJ, USA, 2011).

[3] L. Allen, M. W. Beijersbergen, R. J. C. Spreeuw, and J. P. Woerdman, Orbital angularmomentum of light and the transformation of Laguerre-Gaussian laser modes, *Phys. Rev. A* **45**, 8185 (1992).

[4] J. E. Curtis and D. G. Grier, Structure of optical vortices, *Phys. Rev. Lett.* **90**, 133901 (2003).

[5] B. Thidé, H. Then, J. Sjöholm, K. Palmer, J. Bergman, T. D. Carozzi, Ya. N. Istomin, N. H. Ibragimov, and R. Khamitova, Utilization of photon orbital angular momentum in the low-frequency radio domain, *Phys. Rev. Lett.* **99**, 087701 (2007).

[6] R. Geneaux, A. Camper, T. Auguste, O. Gobert, J. Caillat, R. Taïeb, and T. Ruchon, Synthesis and characterization of attosecond light vortices in the extreme ultraviolet, *Nat. Commun.* **7**, 12583 (2016).

[7] M. Harwit, Photonic orbital angular momentum in astrophysics, *Astrophys*. **556**, A130 (2003).

[8] F. Tamburini, B. Thidé, G. Molina-Terriza, and G. Anzolin, Twisting of light around rotating black hole, *Nat. Phys.* **7**, 195 (2011).

[9] H. He, M. Friese, N. R. Heckenberg, and H. Rubinsztein-Dunlop, Direct observation of transfer of angular momentum to absorptive particles from a laser beam with a phase singularity, *Phys. Rev. Lett.* **75**, 826 (1995).

[10] S.-H. Lee and D. Grier, Giant colloidal diffusivity on corrugated optical vortices. *Phys. Rev. Lett.* **96**, 190601 (2006).

[11] A. Mair, A. Vaziri, G. Weihs, and A. Zeilinger, Entanglement of the orbital angular momentum states of photons, *Nature* **412**, 313 (2001).

[12] R. Fickler, R. Lapkiewicz, W. N. Plick, M. Krenn, C. Schaeff, S. Ramelow, and A. Zeilinger, Quantum entanglement of high angular momenta, *Science* **338**, 640 (2012).

[13] G. Gariepy, J. Leach, K. T. Kim, T. J. Hammond, E. Frumker, R. W. Boyd, and P. B. Corkum, Creating high-harmonic beams with controlled orbital angular momentum, *Phys. Rev. Lett.* **113**, 153901 (2014).

[14] L. Yan, P. Gregg, E. Karimi, A. Rubano, L. Marrucci, R. Boyd, and S. Ramachandran, *Q*-plate enabled spectrally diverse orbital-angular-momentum conversion for stimulated emission depletion microscopy, *Optica* **2**, 900 (2015).

[15] P. Miao, Z. Zhang, J. Sun, W. Walasik, S. Longhi, N. M. Litchinitser, and L. Feng, Orbital angular momentum microlaser, *Science* **353**, 464 (2016).

[16] G. Gibson, J. Courtial, M. J. Padgett, M. Vasnetsov, V. Pas'ko, S. M. Barnett, and S. Franke-Arnold, Free-space information transfer using light beams carrying orbital angular momentum, *Opt. Express* **12**, 5448 (2004).

[17] F. Tamburini, E. Mari, A. Sponselli, B. Thidé, A. Bianchini, and F. Romanato, Encoding many channels on the same frequency through radio vorticity: first experimental test, *New J. Phys.* **14**, 033001 (2012).

[18] Y. Yan, G. Xie, M. P.J. Lavery, H. Huang, N. Ahmed, C. Bao, Y. Ren, Y. Cao, L. Li, Z. Zhao, A. F. Molisch, M. Tur, M. J. Padgett, A. E. Willner, High-capacity millimetre-wave communications with orbital angular momentum multiplexing, *Nat. Commun.* **5**, 4876 (2014).

[19] J. Wang, J.-Y. Yang, I. M. Fazal, N. Ahmed, Y. Yan, H. Huang, Y. Ren, Y. Yue, S. Dolinar, M. Tur, and A. E. Willner, Terabit free-space data transmission employing orbital angular momentum multiplexing, *Nat. Photonics* **6**, 488 (2012).

[20] F. Tamburini, E. Mari, B. Thidé, C. Barbieri, and F. Romanato, Experimental verification of photon angular momemtum and vorticity with radio techniques, *Appl. Phys. Lett.* **99**, 204102 (2011).

[21] M. J. Padgett and L. Allen, Orbital angular momentum exchange in cylindrical-lens mode converters, *J. Opt. B Quantum Semiclass. Opt.* **4**, S17 (2002).

[22] N. R. Heckenberg, R. McDuff, C. P. Smith, and A. G. White, Generation of optical phase singularities by computer-generated holograms, *Opt. Lett.* **17**, 221 (1992).

[23] N. Zhang, X. C. Yuan, and R. E. Burge, Extending the detection range of optical vortices by Dammann vortex gratings, *Opt. Lett.* **35**, 3495 (2010).

[24] X. Cai, J. Wang, M. J. Strain, B. Johnson-Morris, J. Zhu, M. Sorel, J. L. O'Brien, M. G. Thompson, and S. Yu, Integrated compact optical vortex beam emitters, *Science* **338**, 363 (2012).

[25] X.-D. Bai, X.-L. Liang, J.-P. Li, K. Wang, J.-P. Geng, and R.-H. Jin, Rotman lens-based circular array for generating five-mode OAM radio beams, *Sci. Rep.* **6**, 27815 (2016).

[26] M. Barbuto, F. Trotta, F. Bilotti, and A. Toscano, Circular polarized patch antenna generating orbital angular momentum, *Prog. In Electromagn. Res.* **148**, 23-30 (2014).

[27] N. Yu and F. Capasso, Flat optics with designer metasurfaces, *Nat. Mater.* **13**, 139 (2014).

[28] Y. Yang, W. Wang, P. Moitra, I. I. Kravchenko, D. P. Briggs, and J. Valentine, Dielectric meta-reflectarray for broadband linear polarization conversion and optical vortex generation, *Nano Lett.* **14**, 1394 (2014).

[29] S. Yu, L. Li, and G. Shi, Dual-polarization and dual-mode orbital angular momentum radio vortex beam generated by using reflective metasurface, *Appl. Phys. Express* **9**, 082202 (2016).

[30] N. Yu, P. Genevet, M. A. Kats, F. Aieta, J. P. Tetienne, F. Capasso, and Z. Gaburro, Light propagation with phase discontinuities: generalized laws of reflection and refraction, *Science* **334**, 334 (2011).

[31] J. Sun, X. Wang, T. Xu, Z. A. Kudyshev, A. N. Cartwright, and N. M. Litchinitser, Spinning light on the nanoscale. *Nano Lett.* **14**, 2726 (2014).

[32] A. Arbabi, Y. Horie, M. Bagheri, and A. Faraon, Dielectric metasurfaces for complete control of phase and polarization with subwavelength spatial resolution and high transmission, *Nat. Nanotech.* **10**, 937 (2015).

[33] L. Cheng, W. Hong, and Z.-C. Hao, Generation of electromagnetic waves with arbitrary orbital angular momentum modes, *Sci. Rep.* **4**, 4814 (2014).

[34] S. Pancharatnam, Generalized theory of interference, and its applications. Part I. Coherent Pencils, *Proc. Indian Acad. Sci. A*, **44**, 247 (1956).

[35] M. V. Berry, The adiabatic phase and Pancharatnam's phase for polarized light, *J. Mod. Opt.* **34**, 1401 (1987).

[36] K. Y. Bliokh, F. J. Rodríguez-Fortuño, F. Nori, and A. V. Zayats, Spin–orbit interactions of light, *Nat. Photon.* **9**, 796 (2015).

[37] S. Xiao, J. Wang, F. Liu, S. Zhang, X. Yin, and J. Li, Spin-dependent optics with metasurfaces, *Nanophoton*. **6**, 215 (2017).

[38] W. Luo, S. Xiao, Q. He, S. Sun, and L. Zhou, Photonic spin Hall effect with nearly 100% efficiency, *Adv. Opt. Mater.* **3**, 1102 (2015).

[39] A. Shaltout, J. Liu, V. M. Shalaev, and A. V. Kildishev, Optically active metasurface with non-chiral plasmonic nanoantennas, *Nano Lett.* **14,** 4426-4431 (2014).

[40] P. Yu, J. Li, C. Tang, H. Cheng, Z. Liu, Z. Li, Z. Liu, C. Gu, J. Li, S. Chen, and J. Tian, Controllable optical activity with non-chiral plasmonic metasurfaces, *Light Sci. Appl.* **5**, e16096 (2016).

[41] F. Ding, A. Pors, Y. Chen, V. A. Zenin, and S. I. Bozhevolnyi, Beam-size-invariant spectropolarimeters using gap-plasmon metasurfaces, *ACS Photon.* **4**, 943-949 (2017).

[42] A. Shaltout, J. Liu, A. V. Kildishev, and V. M. Shalaev, Photonic spin Hall effect in gap–plasmon metasurfaces for on-chip chiroptical spectroscopy, *Optica* **2**, 860-863 (2015).

[43] S. Choudhury, U. Guler, A. Shaltout, V. M. Shalaev, A. V. Kildishev, and A. Boltasseva, Pancharatnam–Berry phase manipulating metasurface for visible color hologram based on low loss silver thin film, *Adv. Opt. Mater.* **5**, 1700196 (2017).

[44] P. Genevet, F. Capasso, F. Aieta, M. Khorasaninejad, and R. Devlin, Recent advances in planar optics: fromplasmonic to dielectric metasurfaces, *Optica* **4**, 139-152 (2017).

[45] E. Maguid, I. Yulevich, D. Veksler, V. Kleiner, M. L. Brongersma, and E. Hasman, Photonic spin-controlled multifunctional shared-aperture antenna array, *Science* **352**, 1202 (2016).

[46] L. Huang, X. Chen, H. Mühlenbernd, G. Li, B. Bai, Q. Tan, G. Jin, T. Zentgraf, and S. Zhang, Dispersionless phase discontinuities for controlling light propagation, *Nano Lett.* **12**, 5750 (2012).

[47] G. Li, M. Kang, S. Chen, S. Zhang, E. Y.-B. Pun, K. W. Cheah, and J. Li, Spin-enabled plasmonic metasurfaces for manipulating orbital angular momentum of light, *Nano Lett.* **13**, 4148 (2013).

[48] M. Pu, X. Li, X. Ma, Y. Wang, Z. Zhao, C. Wang, C. Hu, P. Gao, C. Huang, H. Ren, X. Li, F. Qin, J. Yang, M. Gu, M. Hong, and X. Luo, Catenary optics for achromatic generation of perfect optical angular momentum, *Sci. Adv.* **1**, e1500396 (2015).

[49] J. Zeng, L. Li, X. Yang, and J. Gao, Generating and separating twisted light by gradient−rotation split-ring antenna metasurfaces, *Nano Lett.* **16**, 3101 (2016).

[50] M. Q. Mehmood, S. Mei, S. Hussain, K. Huang, S. Y. Siew, L. Zhang, T. Zhang, X. Ling, H. Liu, J. Teng, A. Danner, S. Zhang, and C.-W. Qiu, Visible-frequency metasurface for structuring and spatially multiplexing optical vortices, *Adv. Mater.* **28**, 2533 (2016).

[51] D. Veksler, E. Maguid, N. Shitrit, D. Ozeri. V. Kleiner, and E. Hasman, Multiple wavefront shaping by metasurface based on mixed random antenna groups, *ACS Photon.* **2**, 661 (2015).

[52] A. A. Tahir, S. A. Schulz, I. De Leon, and R. W. Boyd, Design principles for wave plate metasurfaces using plasmonic L-shaped nanoantennas, *J. Opt.* **19**, 035001 (2017).

[53] F. Monticone, N. M. Estakhri, and A. Alù, Full control of nanoscale optical transmission with a composite meta-screen, *Phys. Rev. Lett.* **110**, 203903 (2013).

[54] X. Ding, F. Monticone, K. Zhang, L. Zhang, D. L. Gao, S. N. Burokur, A.de Lustrac, Q. Wu, C. W. Qiu, and A. Alù, Ultrathin Pancharatnam-Berry metasurface with maximal cross-polarization efficiency, *Adv. Mater.* **27**, 1195 (2015).

[55] L. Zhou, W. Wen, C. Chan, and P. Sheng, Electromagnetic- wave tunneling through negative-permittivity media with high magnetic fields, *Phys. Rev. Lett.* 94, 243905 (2005).

[56] V. S. Asadchy, I. A. Faniayeu, Y. Radi, S. A. Khakhomov, I. V. Semchenko, and S. A. Tretyakov, Broadband reflectionless metasheets: frequency-selective transmission and perfect absorption, *Phys. Rev. X* **5**, 031005 (2015).

[57] Z. Li, W. Liu, H. Cheng, J. Liu, S. Chen, and J. Tian, Simultaneous generation of high-efficiency broadband asymmetric anomalous refraction and reflection waves with few-layer anisotropic metasurface, *Sci. Rep.* **6**, 35485 (2016).

[58] C. Pfeiffer and A. Grbic, Controlling vector Bessel beams with metasurfaces, *Phys. Rev. Appl.* **2**, 044012 (2014).

[59] W. C. Chew, *Waves and Fields in Inhomogeneous Media*, (Van Nostrand Reinhold, 1990).

[60] See Supplemental Material for the scattering properties of triple-layered AIS structure, unit cell design for the mid-infrared regime, diffraction analysis of the gradient PB transmit-array, hybrid simulation of finite PB transmit-arrays, simulation results of the single-mode vortex beam generator, measurement setup and details, and additional simulations of direction, mode, and intensity ratio controllability.

[61] W. Luo, S. Xiao, Q. He, S. Sun, and L. Zhou, Transmissive ultrathin Pancharatnam-Berry metasurfaces with nearly 100% efficiency, *Phys. Rev. Appl.* **7**, 044033 (2017).

[62] Z. H. Jiang, P. E. Sieber, L. Kang, and D. H. Werner, Restoring intrinsic properties of electromagnetic radiators using ultralightweight integrated metasurface cloaks, *Adv. Funct. Mater.* **25**, 4708 (2015).

[63] Z. H. Jiang, L. Kang, and D. H. Werner, Conformal metasurface-coated dielectric waveguides for highly confined broadband optical activity with simultaneous low-visibility and reduced crosstalk, *Nat. Commun.* **8**, 356 (2017).

[64] S. Chen, Y. Cai, G. Li, S. Zhang, and K. W. Cheah, Geometric metasurface fork gratings for vortex-beam generation and manipulation, *Laser Photon. Rev.* **10**, 322 (2016).

[65] J. Albero, I. Moreno, J. A. Davis, D. M. Cottrell, and D. Sand, Generalized phase diffraction gratings with tailored intensity, *Opt. Lett.* **37**, 4227 (2012).

[66] T. Lei, M. Zhang, Y. Li, P. Jia, G. N. Liu, X. Xu, Z. Li, C. Min, J. Lin, C. Yu, H. Niu, and X. Yuan, Massive individual orbital angular momentum channels for multiplexing enabled by Dammann gratings, *Light Sci. Appl.* **4**, e257 (2015).

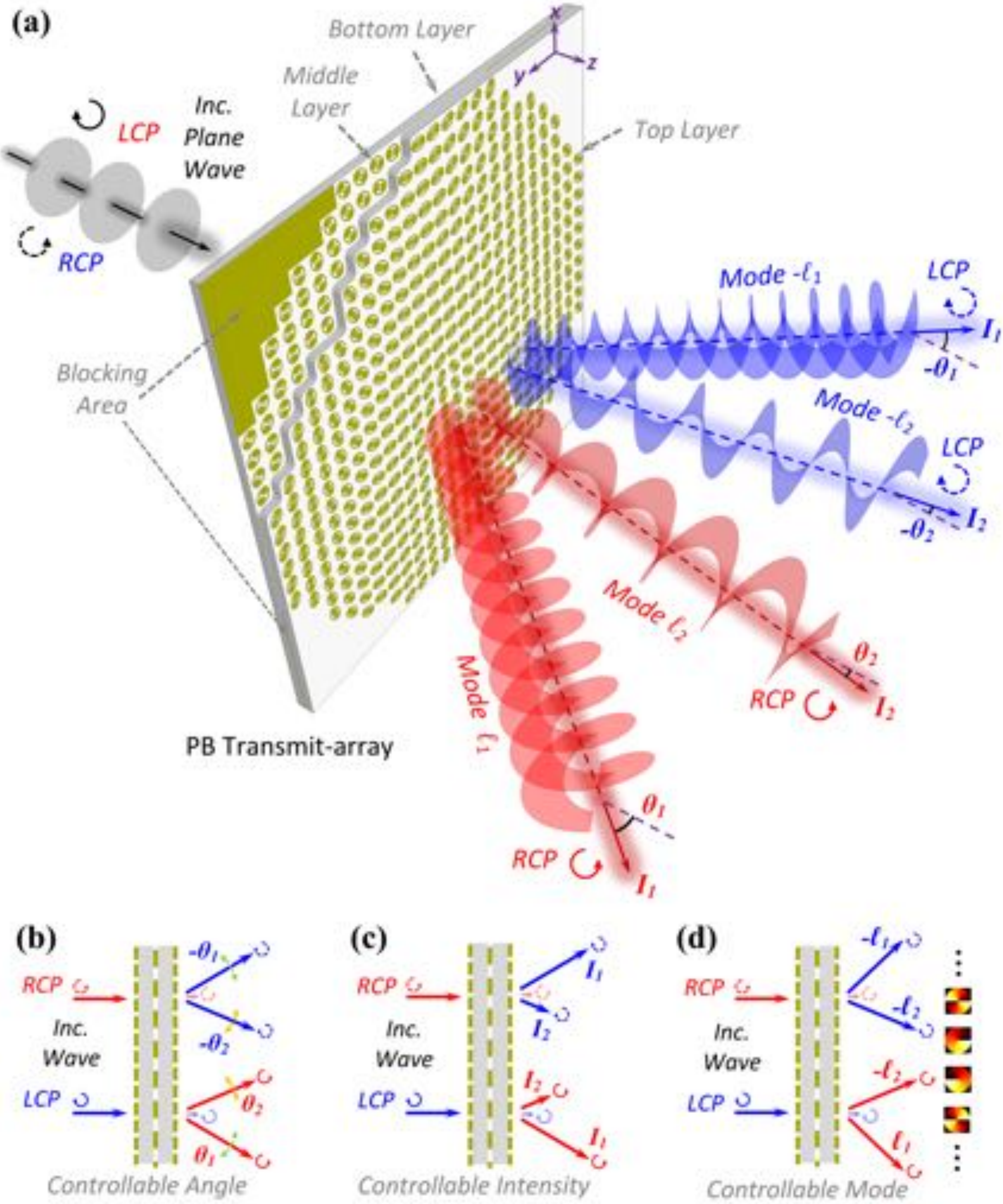
(a)
Bottom Layer
x
y
z
Middle Layer
Top Layer
LCP
Inc.
Plane
Wave
RCP
Mode $-\ell_1$
LCP
I_1
$-\theta_1$
Mode $-\ell_2$
LCP
I_2
$-\theta_2$
Blocking Area
Mode ℓ_2
θ_2
RCP
I_2
Mode ℓ_1
θ_1
RCP
I_1
PB Transmit-array
(b)
RCP
$-\theta_1$
Inc.
Wave
$-\theta_2$
LCP
θ_2
θ_1
Controllable Angle
(c)
RCP
I_1
I_2
Inc.
Wave
LCP
I_2
I_1
Controllable Intensity
(d)
RCP
$-\ell_1$
$-\ell_2$
Inc.
Wave
LCP
$-\ell_2$
ℓ_1
Controllable Mode

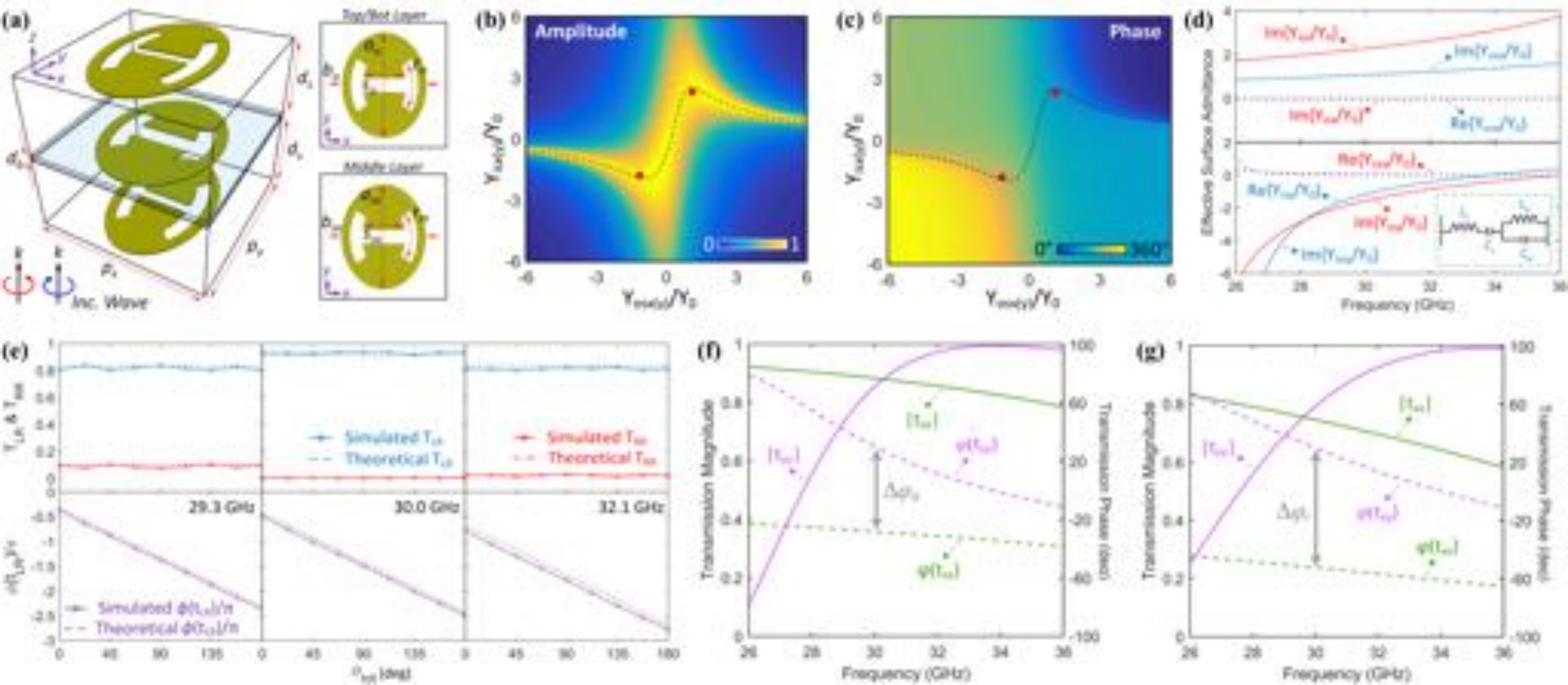
(a)
Top/Bot Layer
Middle Layer
Inc. Wave
(b)
Amplitude
Y_{ind(x)}/Y_0
Y_{ind(y)}/Y_0
0
1
(c)
Phase
0°
360°
(d)
Effective Surface Admittance
Frequency (GHz)
Im{Y_{ind}/Y_0}
Re{Y_{ind}/Y_0}
L_1
L_2
C_1
C_2
(e)
T_{LR} & T_{RR}
Simulated T_{LR}
Theoretical T_{LR}
Simulated T_{RR}
Theoretical T_{RR}
29.3 GHz
30.0 GHz
32.1 GHz
Simulated φ(t_{LR})/π
Theoretical φ(t_{LR})/π
θ_{rot} (deg)
(f)
Transmission Magnitude
Transmission Phase (deg)
Frequency (GHz)
|t_{xx}|
|t_{yy}|
φ(t_{xx})
φ(t_{yy})
Δφ_0
(g)
Transmission Magnitude
Transmission Phase (deg)
Frequency (GHz)
|t_{xx}|
|t_{yy}|
φ(t_{xx})
φ(t_{yy})
Δφ_1

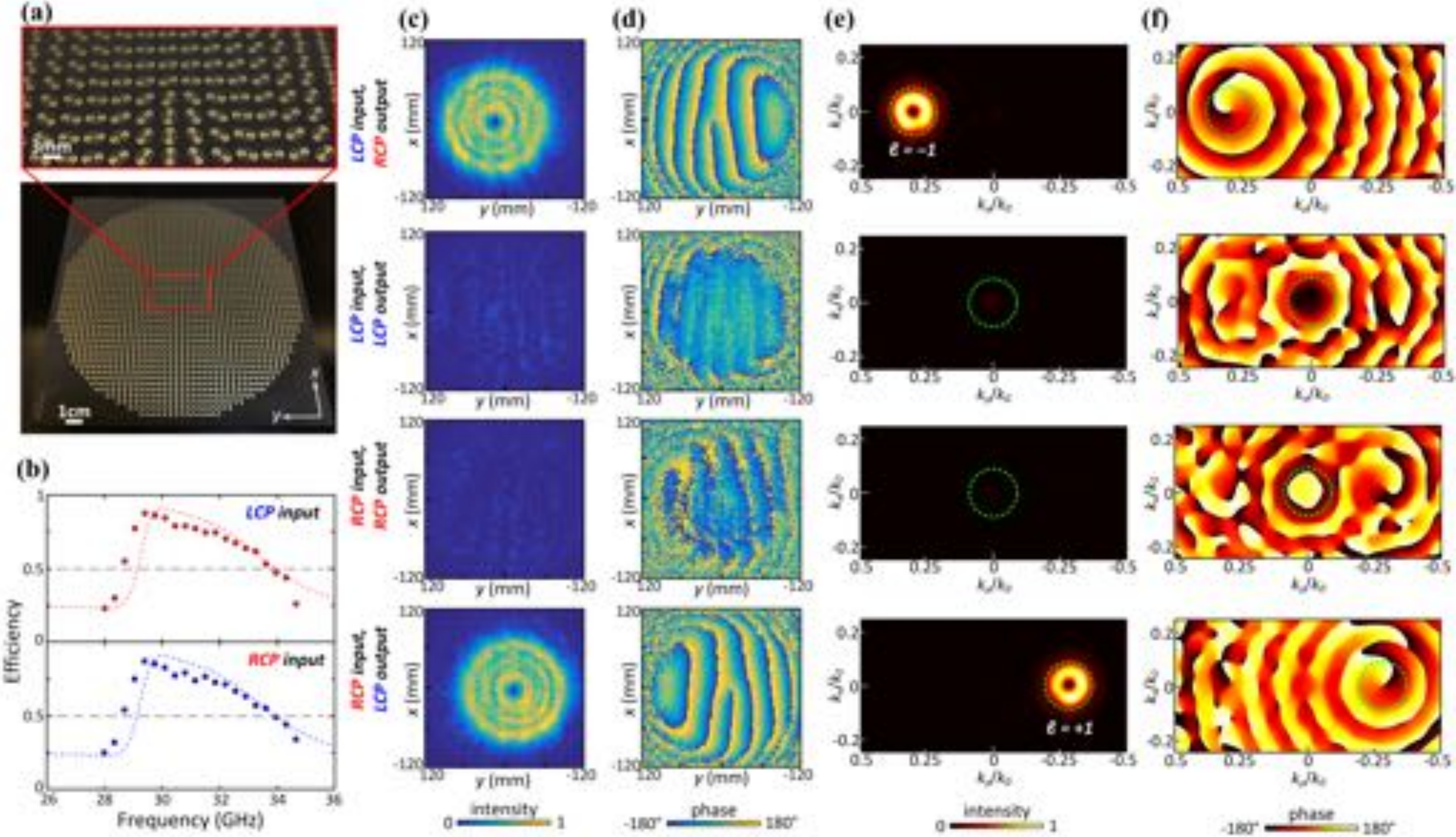
(a)
5mm
1cm
x
y
(b)
LCP input
RCP input
Efficiency
Frequency (GHz)
0
0.5
1
26
28
30
32
34
36
(c)
LCP input, RCP output
LCP input, LCP output
RCP input, RCP output
RCP input, LCP output
x (mm)
y (mm)
120
-120
intensity
0
1
(d)
phase
-180°
180°
(e)
k_x/k_0
k_y/k_0
0.2
0
-0.2
0.5
0.25
-0.25
-0.5
ℓ = −1
ℓ = +1
intensity
0
1
(f)
phase
-180°
180°

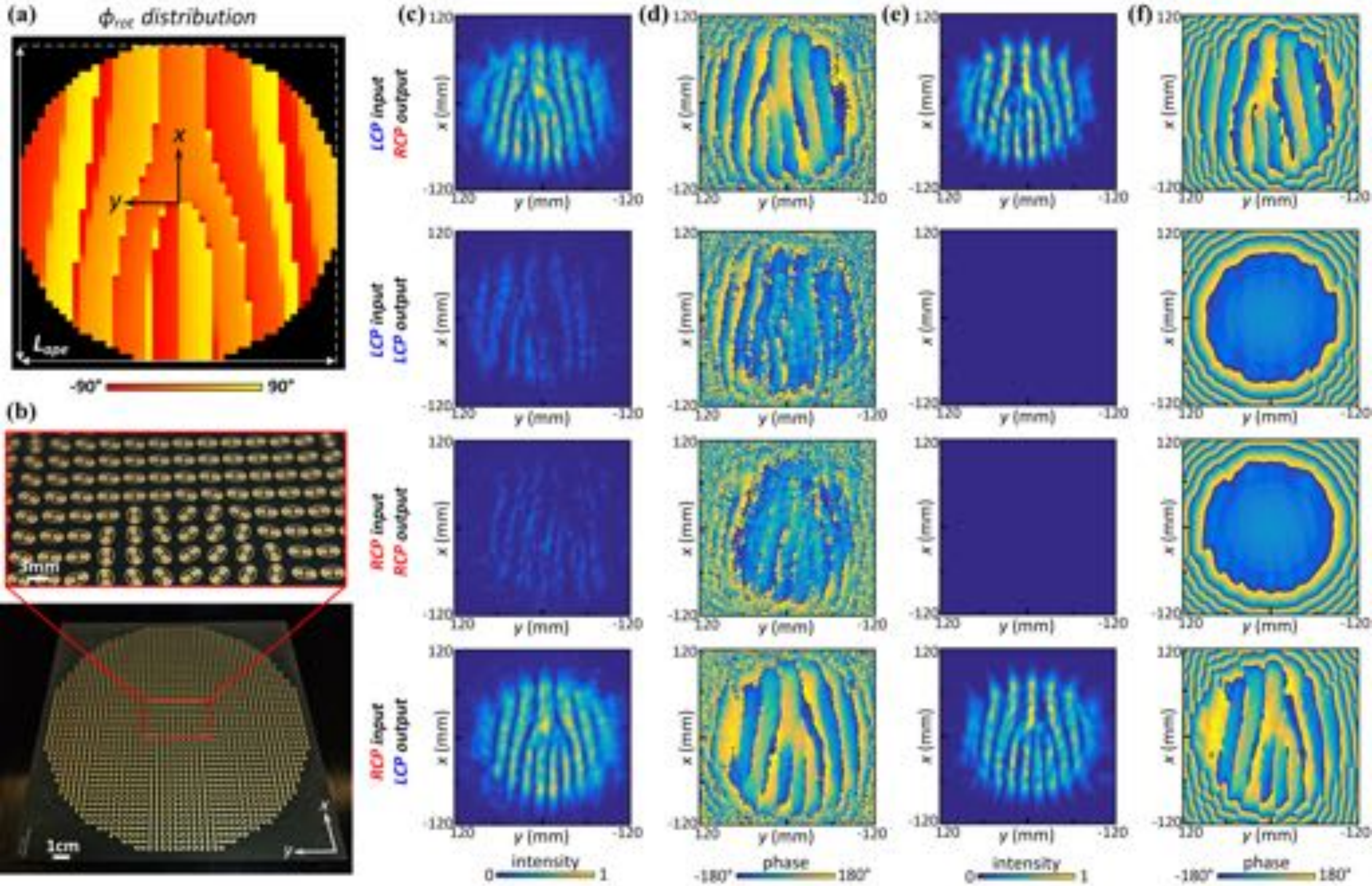
(a)
φrot distribution
x
y
Lape
-90°
90°
(b)
1mm
1cm
x
y
(c)
(d)
(e)
(f)
LCP input
RCP output
LCP input
LCP output
RCP input
RCP output
RCP input
LCP output
120
-120
x (mm)
y (mm)
intensity
0
1
phase
-180°
180°

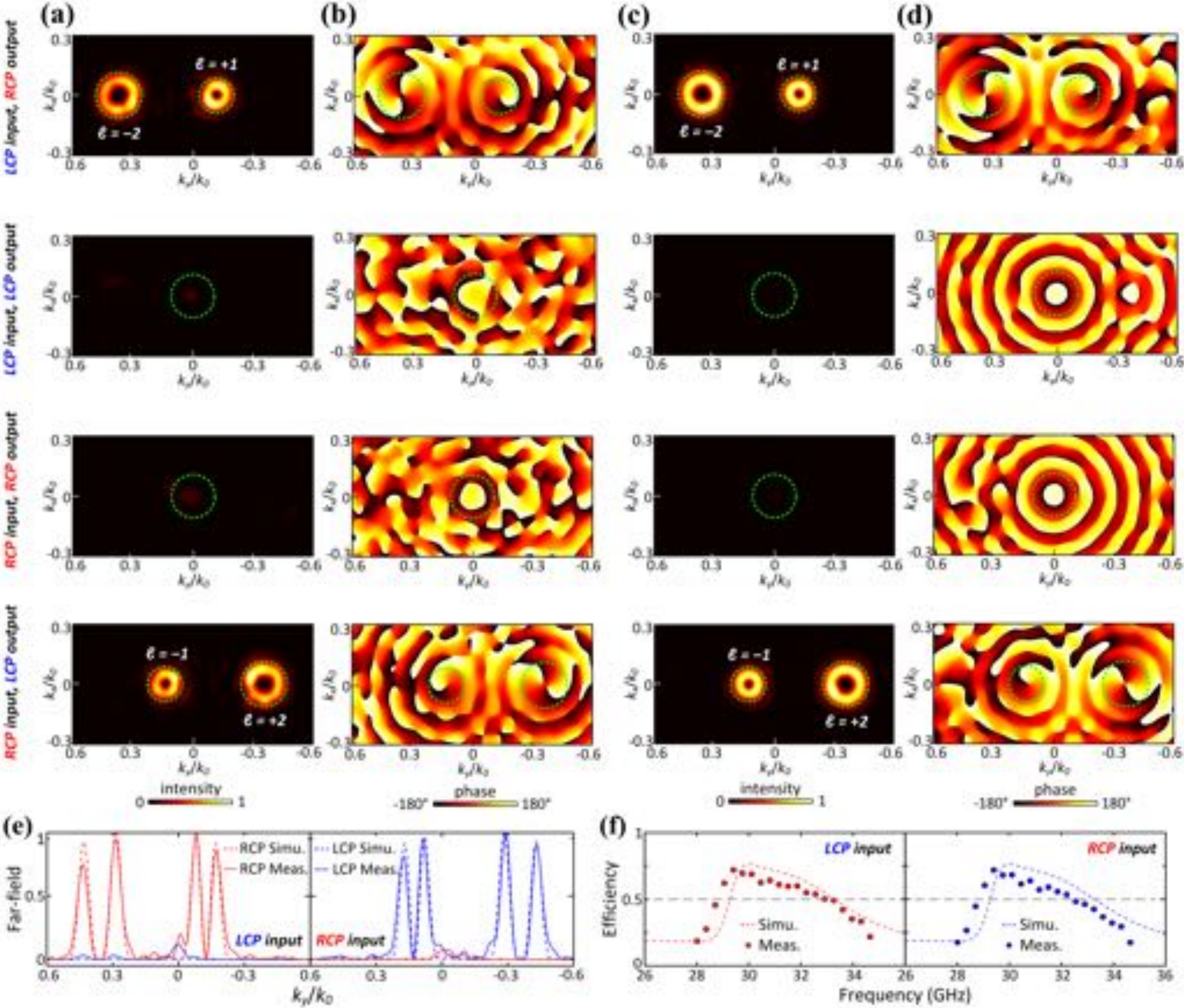
(a)
(b)
(c)
(d)
LCP input, RCP output
LCP input, LCP output
RCP input, RCP output
RCP input, LCP output
ℓ = +1
ℓ = −2
ℓ = −1
ℓ = +2
k_x/k_0
k_y/k_0
0.3
0
-0.3
0.6
-0.6
intensity
0
1
phase
-180°
180°
(e)
Far-field
RCP Simu.
RCP Meas.
LCP Simu.
LCP Meas.
LCP input
RCP input
0.5
(f)
Efficiency
LCP input
RCP input
Simu.
Meas.
Frequency (GHz)
26
28
30
32
34
36

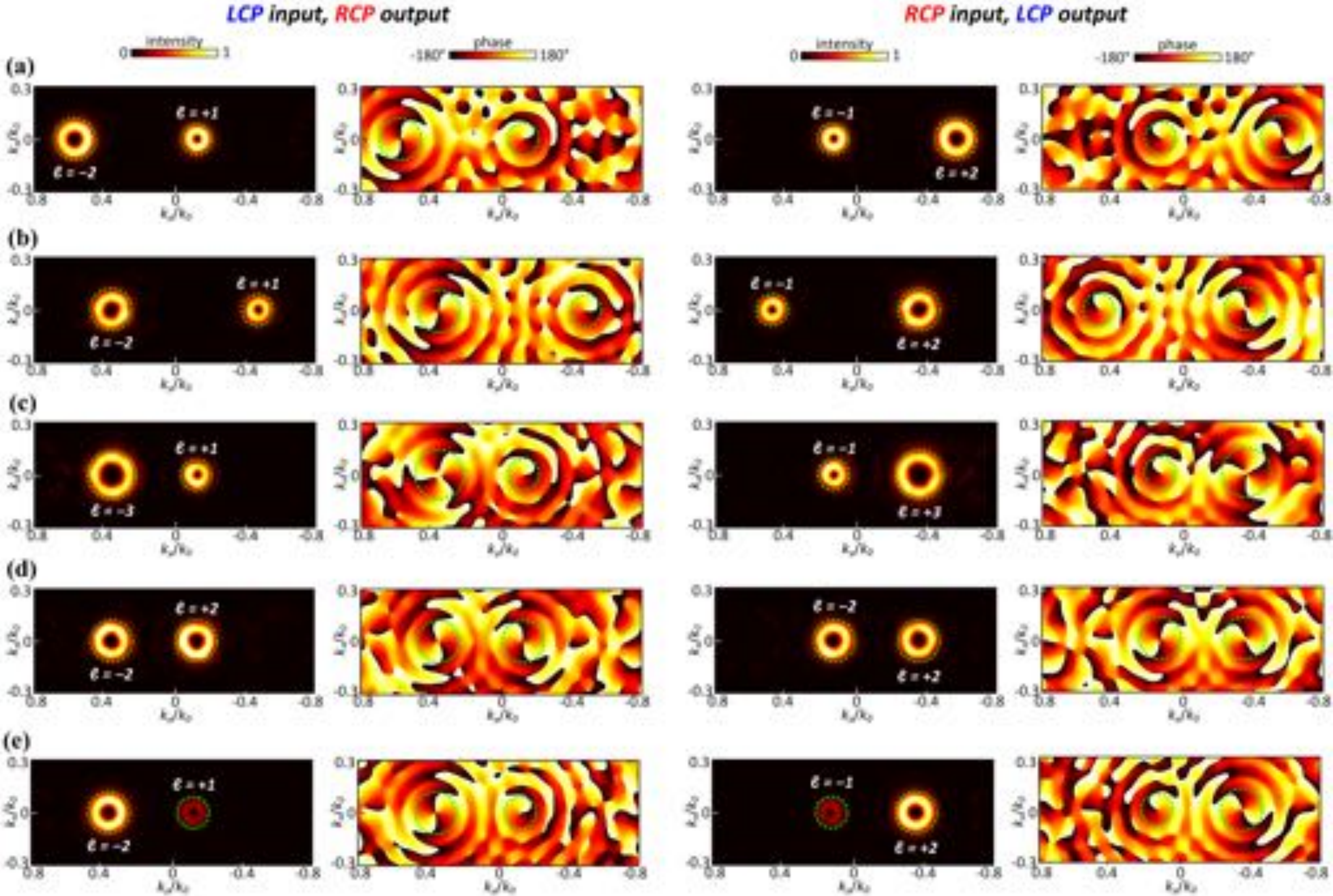
LCP input, RCP output
RCP input, LCP output
intensity
0
1
phase
-180°
180°
(a)
(b)
(c)
(d)
(e)
ℓ = +1
ℓ = −2
ℓ = −1
ℓ = +2
ℓ = −3
ℓ = +3
ℓ = +2
ℓ = −2
0.3
0
-0.3
0.8
0.4
0
-0.4
-0.8
k_x/k_0
k_y/k_0

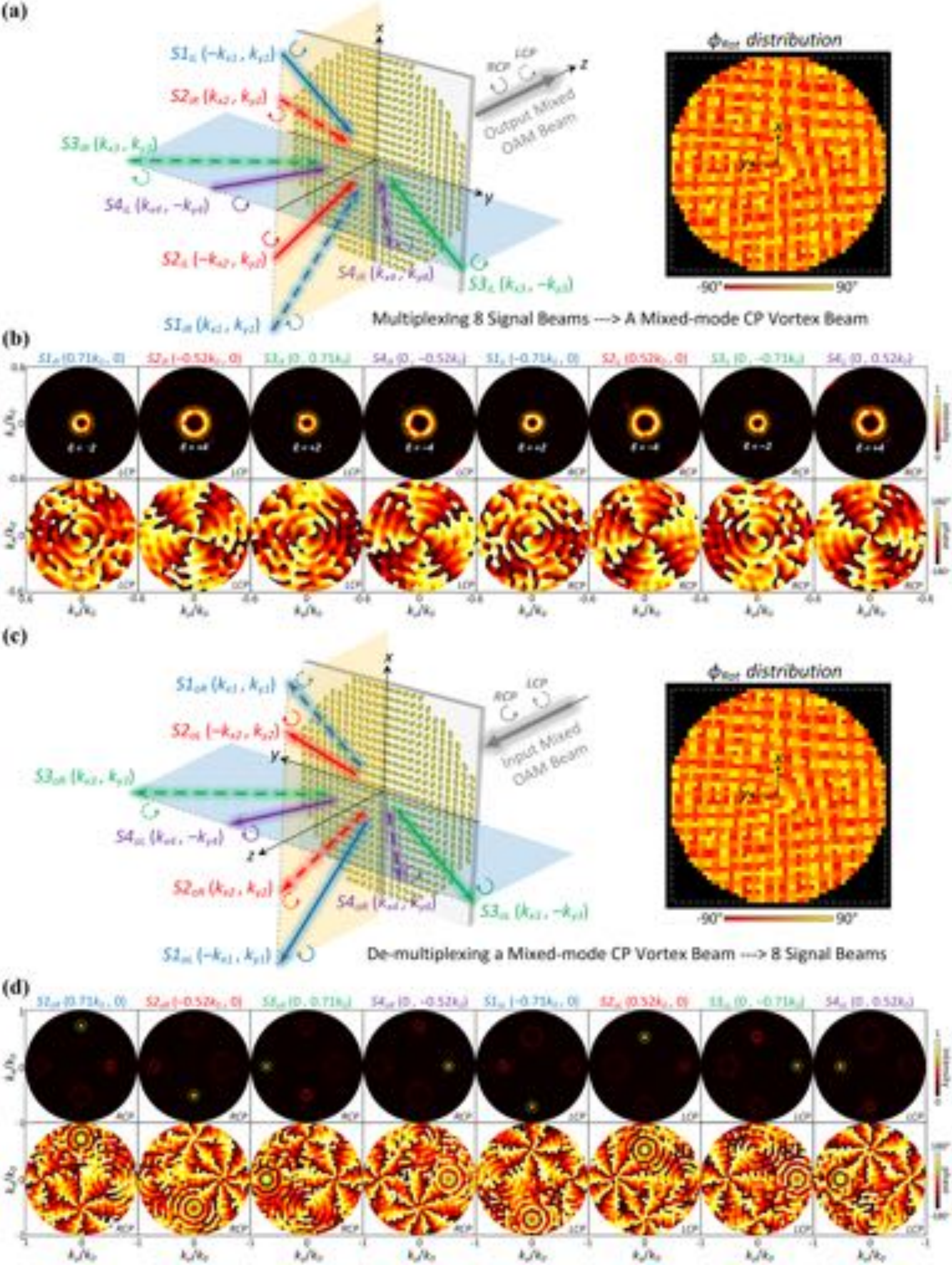
(a)
$S1_{iL}\,(-k_{x1}, k_{y1})$
$S2_{iR}\,(k_{x2}, k_{y2})$
$S3_{iR}\,(k_{x3}, k_{y3})$
$S4_{iL}\,(k_{x4}, -k_{y4})$
$S2_{iL}\,(-k_{x2}, k_{y2})$
$S4_{iR}\,(k_{x4}, k_{y4})$
$S3_{iL}\,(k_{x3}, -k_{y3})$
$S1_{iR}\,(k_{x1}, k_{y1})$
x
y
z
RCP
LCP
Output Mixed OAM Beam
ϕ_{Rot} distribution
-90°
90°
Multiplexing 8 Signal Beams ---> A Mixed-mode CP Vortex Beam
(b)
$S1_{R}\,(0.71k_0, 0)$
$S2_{R}\,(-0.52k_0, 0)$
$S3_{R}\,(0, 0.71k_0)$
$S4_{R}\,(0, -0.52k_0)$
$S1_{L}\,(-0.71k_0, 0)$
$S2_{L}\,(0.52k_0, 0)$
$S3_{L}\,(0, -0.71k_0)$
$S4_{L}\,(0, 0.52k_0)$
$\ell = -2$
$\ell = +4$
$\ell = +2$
$\ell = -4$
$\ell = +2$
$\ell = -4$
$\ell = -2$
$\ell = +4$
LCP
RCP
k_y/k_0
k_x/k_0
Amplitude
Phase
180°
-180°
(c)
$S1_{oR}\,(k_{x1}, k_{y1})$
$S2_{oL}\,(-k_{x2}, k_{y2})$
$S3_{oR}\,(k_{x3}, k_{y3})$
$S4_{oL}\,(k_{x4}, -k_{y4})$
$S2_{oR}\,(k_{x2}, k_{y2})$
$S4_{oR}\,(k_{x4}, k_{y4})$
$S3_{oL}\,(k_{x3}, -k_{y3})$
$S1_{oL}\,(-k_{x1}, k_{y1})$
x
y
z
RCP
LCP
Input Mixed OAM Beam
ϕ_{Rot} distribution
-90°
90°
De-multiplexing a Mixed-mode CP Vortex Beam ---> 8 Signal Beams
(d)
$S1_{R}\,(0.71k_0, 0)$
$S2_{R}\,(-0.52k_0, 0)$
$S3_{R}\,(0, 0.71k_0)$
$S4_{R}\,(0, -0.52k_0)$
$S1_{L}\,(-0.71k_0, 0)$
$S2_{L}\,(0.52k_0, 0)$
$S3_{L}\,(0, -0.71k_0)$
$S4_{L}\,(0, 0.52k_0)$
RCP
LCP
k_y/k_0
k_x/k_0
Amplitude
Phase
180°
-180°